

3D incoherent imaging using an ensemble of sparse self-rotating beams

ANDREI-IOAN BLEAHU,^{1,†} SHIVASUBRAMANIAN GOPINATH,^{1,†}
TAUNO KAHRO,¹ PRAVEEN PERIYASAMY ANGAMUTHU,¹ ARAVIND
SIMON JOHN FRANCIS RAJESWARY,¹ SHASHI PRABHAKAR,^{2,†} 
RAVI KUMAR,³  GANGI REDDY SALLA,³ RAVINDRA P. SINGH,² 
KAUPO KUKLI,¹ AILE TAMM,¹ JOSEPH ROSEN,⁴  AND
VIJAYAKUMAR ANAND^{1,5,*} 

¹*Institute of Physics, University of Tartu, W. Ostwald 1, 50411 Tartu, Estonia*

²*Quantum Science and Technology Laboratory, Physical Research Laboratory, Navrangpura, Ahmedabad-380009, India*

³*Department of Physics, SRM University-AP, Amaravati 522502, Andhra Pradesh, India*

⁴*School of Electrical and Computer Engineering, Ben-Gurion University of the Negev, Beer-Sheva 8410501, Israel*

⁵*Optical Sciences Center and ARC Training Centre in Surface Engineering for Advanced Materials (SEAM), School of Science, Computing and Engineering Technologies, Optical Sciences Center, Swinburne University of Technology, Hawthorn, Melbourne, VIC 3122, Australia*

[†]The authors contributed equally to this work

* vijayakumar.anand@ut.ee

Abstract: Interferenceless coded aperture correlation holography (I-COACH) is one of the simplest incoherent holography techniques. In I-COACH, the light from an object is modulated by a coded mask, and the resulting intensity distribution is recorded. The 3D image of the object is reconstructed by processing the object intensity distribution with the pre-recorded 3D point spread intensity distributions. The first version of I-COACH was implemented using a scattering phase mask, which makes its implementation challenging in light-sensitive experiments. The I-COACH technique gradually evolved with the advancement in the engineering of coded phase masks that retain randomness but improve the concentration of light in smaller areas in the image sensor. In this direction, I-COACH was demonstrated using weakly scattered intensity patterns, dot patterns and recently using accelerating Airy patterns, and the case with accelerating Airy patterns exhibited the highest SNR. In this study, we propose and demonstrate I-COACH with an ensemble of self-rotating beams. Unlike accelerating Airy beams, self-rotating beams exhibit a better energy concentration. In the case of self-rotating beams, the uniqueness of the intensity distributions with depth is attributed to the rotation of the intensity pattern as opposed to the shifts of the Airy patterns, making the intensity distribution stable along depths. A significant improvement in SNR was observed in optical experiments.

© 2023 Optica Publishing Group under the terms of the [Optica Open Access Publishing Agreement](#)

1. Introduction

Imaging technology consists of a collection of methods that reproduce images of objects between different domains [1]. One of the most widely used imaging technologies is digital imaging. In digital imaging, physical objects are imaged in an optical step and a digital step [2]. The procedures undertaken for each step can be described as follows. First, light scattered by an object is modulated by a lens and incident on an image sensor. Second, the optically generated intensity pattern sensed by an image sensor is read by computer software to obtain the object's image. The above digital imaging is termed direct digital imaging if the optically generated pattern is an image of the object. In some cases of digital imaging, the optical modulator generates an

intensity pattern that is not an image of the object. In such cases, an additional computational process called image reconstruction is required to complete the imaging process. The imaging of objects via an intermediate nonimage recorded pattern constitutes indirect digital imaging.

A typical example of indirect digital imaging is digital holography (DH) [3]. DH can be described as the discrete recording, digital storage, and numerical reconstruction of optical wavefronts [4]. In DH, a camera records one or a few digital holograms of an object by wave interference of the object and reference waves. The holograms are then used to reconstruct the object's image through computational reconstruction procedures. As DH uses more complicated and costlier setups to create interference, unlike direct digital imaging, it is necessary to justify the above by clear advantages. One of the main advantages of using DH instead of direct imaging is its ability to record and reconstruct a complete 3D image of the object with one or a few camera shots. Since most of the imaging tasks in optics are produced with natural incoherent light, an important subset of DH techniques is represented by incoherent digital holography (IDH).

Incoherent digital holography (IDH) techniques began to emerge at the end of the 20th century with advances in astronomical and biomedical imaging [5]. The optical configuration of a typical IDH is relatively more complicated in comparison to coherent light-based DH [6,7]. With coherent light, the light from an object interferes with a reference wave to create a hologram. This simple wave interference is not possible in IDH. As such, an interference between the reference and object wave will not create a stable interference pattern due to the lack of spatial coherence between the waves. Hence, in IDH, the digital hologram is recorded based on the self-interference principle. Light from an object point is coherent with respect to itself, which means that if a replica of the point can be created, then the light from the point and that from its replica can coherently interfere. A notable IDH technique based on the self-interference principle called Fresnel incoherent correlation holography (FINCH) was proposed and demonstrated in 2007 [8,9]. Notably, FINCH does not satisfy the Lagrange invariant condition and exhibits a superior lateral resolution compared to direct incoherent digital imaging [10]. The non-classical high-lateral resolution of FINCH is one of the main reasons why this system is widely used. The use of incoherent light makes FINCH suitable for fluorescence microscopy and astronomical imaging [9].

FINCH does have weaknesses – lower axial and temporal resolutions than direct incoherent digital imaging – and research has been focused on improving those limitations [11–14]. In addition, FINCH requires two-wave interference, leading to a complicated setup with several optical components, such as lenses, polarizers, and active devices, to create phase-shifted holograms. An alternative method of the IDH technique based on the self-interference principle is coded aperture correlation holography (COACH) [15]. In FINCH, light from an object point is modulated by two quadratic phase masks with different focal lengths, and the two generated waves interfere. In COACH, light from an object point is modulated by a random phase mask and interferes with an unmodulated light from the same object point. Furthermore, in FINCH, the object's image is reconstructed by numerical back propagation, but in COACH, the object hologram is cross-correlated with the point spread hologram (PSH) recorded at a particular axial plane to reconstruct the object's image at that plane. In a way, COACH can be considered a generalization of FINCH, as a random phase mask is used instead of the quadratic phase mask in FINCH. Therefore, FINCH and COACH have different imaging characteristics. COACH has a lateral resolution and signal-to-noise ratio (SNR) lower than those of FINCH but a relatively higher axial resolution than that of FINCH [16].

It was later identified in COACH that the 3D location information of an object is present in the intensity pattern obtained by modulating the object wave by the random phase mask even before the interference is created. This technique is called interferenceless COACH (I-COACH) [17]. The I-COACH method opened a new pathway for holography, as this optical configuration functions without two-beam interference, unlike any existing IDH techniques. Consequently, the

optical configuration of I-COACH is simple, and the experimental complexity is low, resulting in a significantly lower cost than both FINCH and COACH. I-COACH consisted of a quasi-random phase mask and an image sensor separated by a distance. The imaging procedure is similar to COACH, where the PSH is recorded in addition to the object hologram to reconstruct the object's image by a cross-correlation. The initial correlation methods using matched and phase-only filters demanded multiple camera recordings to achieve a reasonable SNR in I-COACH. An improved computational reconstruction method called nonlinear reconstruction (NLR) was developed that enabled single shot capability in I-COACH with a better SNR [18]. The SNR of I-COACH, even with NLR, was still lower than that of FINCH and direct incoherent digital imaging methods due to the scattering of light. Modified approaches were tried for I-COACH replacing the scattered intensity distribution with randomly located dots [19] and ring patterns [20]. The problem with the above approaches is the need for extensive multiplexing of coded apertures to image different planes of the object [19,21].

A different approach to overcome the limitations of I-COACH is to focus on engineering deterministic optical fields for 3D imaging [22]. One example of an interesting field can be found in a recent study demonstrated using speckle patterns formed by the random interferences of Bessel beams. In that study, the possibility of tuning the axial resolution while keeping the lateral resolution constant was demonstrated [23]. However, again, the SNR was low in that study due to scattering. Another interesting class of beams for 3D imaging are Airy beams [24–26], which are non-diffractive by nature but create unique PSHs even with few diverse beams, unlike the case with Bessel beams [23]. As scattering-based imaging requires a high photon budget, a proof-of-concept 3D incoherent imaging study using a single double-helix beam was recently demonstrated [27]. A recently developed computational reconstruction method called the Lucy-Richardson-Rosen algorithm was applied to a double-helix beam, and a high-quality reconstruction was obtained in the simulation [28]. However, the computational method was highly sensitive to shift errors between the PSH and object hologram, which significantly affected the experimental results. However, the double-helix beam and NLR were not ideally compatible for 3D imaging applications.

Closely related to spiral beams, self-rotating beams have been considered recently for various applications, including optical trapping due to their carrying orbital angular momentum [29]. One of the most interesting properties of such beams is their self-healing property, which can be useful for penetrating obstacles for optical trapping [30]. In recent studies, self-rotating beams were constructed using enormous topological charge values of $\sim 10^6$, and such values carry little physical significance [29,30]. In this study, we propose a sparse array of diffractive lenses with azimuthally varying focal lengths with different rotational frequencies for generating an ensemble of self-rotating beams. The rationale for employing an ensemble of sparse self-rotating beams for 3D imaging applications is rooted in the fundamental requirement of indirect 3D incoherent imaging. To indirectly image multiple planes in I-COACH with a high SNR, the intensity distributions at the sensor plane need to be sparse, intense and at the same time vary with axial locations, retaining the previous two properties. In the case of the first version of I-COACH, the intensity distribution was scattered, so it fulfilled only the final requirement, which is the change in intensity distribution with axial location [17]. In the case of dots [19], they were sparse and intense only for a plane constrained within the depth of focus of the beam, and their intensity was diluted at other planes. The case with Airy beams was better than the two cases mentioned above, as the intensity distribution was sparse and varied with axial location, but the localized intensity was not high due to the larger distribution [31]. Additionally, there is a possibility for the beams to expand beyond the physical size of the sensor [24–26]. The proposed configuration with self-rotating beams has the same longitudinal axes for individual diffractive lenses and satisfies all the above three conditions. Therefore, I-COACH with self-rotating beams is expected to have a better SNR in comparison to Airy beams. In this study, an ensemble of sparse self-rotating

beams generated from spatially incoherent illumination has been implemented in I-COACH for the first time. The performance of the modified I-COACH has been compared with the existing methods of I-COACH, which include the latest developments.

The remainder of this manuscript is organized as follows. Section two describes the theoretical analysis and the methodology. In the third section, the design procedure and simulation results are presented. The experimental procedure and the results are described in the fourth section, followed by the conclusion in the final section.

2. Materials and methods

The proposed 3D incoherent imaging technique is based on the characteristics of a self-rotating beam. However, unlike the recently reported beams generated by phase elements with enormous topological charge values [29,30], a simpler and direct approach is considered. Fresnel zone lenses (FZLs), in general, are designed for collecting and focusing light to a point on the optical axis located at a distance of focal length from the FZL [32]. It is possible to design an FZL to focus light along a relatively short line in the optical axis, and such a lens is called an axilens [33,34], which is often considered an intermediate between an FZL and an axicon [35]. In the axilens and axicon, the radius of the beam-generating element is mapped to the focal path, where every radial section collects light and focuses it at a different distance. Previous studies on Bessel speckles using axicon-based diffractive elements exhibited a low SNR [23]. In this research, the focal distance is dependent upon the azimuthal angle, where every angular section focuses light at a different distance [36]. A similar line focus is obtained as in the case of the axilens and axicon, but the *radial symmetry is broken*, resulting in asymmetric intensity distributions. This type of FZL is termed an FZL with azimuthally variable focus (FZL-AVF).

The optical configuration of imaging using FZL-AVF is shown in Fig. 1(a). FZL needs to be designed for finite conjugate mode or infinite conjugate mode differently depending upon the numerical aperture (NA) [37]. However, when the NA is low, a paraxial approximation can be applied. Hence, the FZL designed for the infinite conjugate mode can be used for imaging in the finite conjugate mode using the well-known focal length relation $\frac{1}{f} = \frac{1}{z_s} + \frac{1}{z_i}$, where z_s and z_i are the object and image distances and f is the focal length. It can be seen from [37] that such an approximation can cause significant spherical aberration if the NA is high and does not satisfy the paraxial approximation. The expression for the focal length of the FZL-AVF is given as

$$f(\theta) = f_0 + \frac{\Delta f}{2\pi}\theta, \quad (1)$$

where f_0 is the minimum focal length and Δf is the focal depth. The diffractive element is divided azimuthally, where every infinitesimal sector focuses light at a distance between f_0 and $f_0 + \Delta f$. Similar to axilens and axicon [33–35], the light from other sectors that do not meet the imaging condition $\frac{1}{f(\theta)} = \frac{1}{z_s} + \frac{1}{z_i}$ forms a blurred image with the degree of blur increasing with an increase in the difference between $f(\theta_1)$ and $f(\theta_2)$. The image magnification of the system varies from $M_1 = z_i[f(2\pi)]/z_s$ to $M_2 = z_i[f(0)]/z_s$, where $z_i(\theta) = \left(\frac{1}{f(\theta)} - \frac{1}{z_s}\right)^{-1}$. Consequently, the image at any plane is not a perfect image of the object as obtained using a regular FZL. The intensity of the maxima at any plane is inversely proportional to Δf . The phase of the diffractive optical element with paraxial approximation can be written as

$$\Phi_{FZL-AVF}(R, \theta) \approx \frac{-2\pi^2 R^2}{\lambda(2\pi f_0 + \Delta f\theta)}. \quad (2)$$

The axial intensity distribution is not a line focus but a self-rotating distribution around the optical axis. When the imaging condition is satisfied for a point located at z_s , a point image is obtained at $z_i(\theta_1)$ by the corresponding sector. However, the sectors with phase distributions

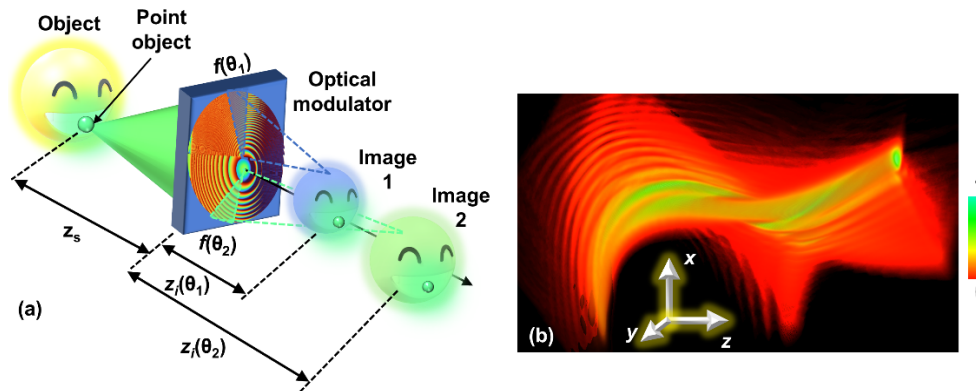


Fig. 1. (a) Optical configuration of imaging using FZL-AVF. (b) 3D axial intensity distribution generated by the FZL-AVF.

that do not meet the imaging condition form a noise pattern in that plane. This noise pattern's orientation changes with axial distance as the location of the contributions of the signal and noise varies for every axial location. The axial distribution of the intensity pattern is shown in Fig. 1(b). It can be seen that the intensity distribution is not a point at any plane but a larger intensity distribution that changes angle with axial location of the point. Therefore, the image formed by such a lens will be distorted, and the distortion direction changes with the axial location of the object and the location of the image sensor. The phase distribution given by Eq. (2) is continuous $[0, 2\pi]$ and thus has a maximum diffraction efficiency of 100%. However, depending upon the implementation method either using an SLM or elements manufactured using lithography methods, the diffraction efficiency will vary.

In this research, four FZL-AVF elements with different longitudinal axes and rotation rates are multiplexed using the random multiplexing method to obtain unique intensity distributions corresponding to different axial locations [8]. The only requirement in selecting the characteristics of self-rotating beams is that the direction of distortion for the four beams should be chaotic to avoid correlation peaks generated due to similarities. A regular summation of complex amplitudes of different FZL-AVF elements would result in a complex function that is difficult to manufacture using lithography techniques or to display on active devices such as spatial light modulators. The proposed random multiplexing approach retains the phase-only configuration at the expense of background noise. The first version of I-COACH used quasi-random phase masks to scatter light. Later, in [19], dot patterns were used to demonstrate I-COACH, and an inverse relation was observed between the number of beams and SNR. Therefore, to achieve a high SNR in I-COACH, an ensemble of sparse beams is needed. In [23] and [31], the possibility of tuning axial resolution independent of lateral resolution was identified. In this study, four beams are considered, as the corresponding axial resolution is similar to that of a lens with the same NA. The phase mask obtained by random multiplexing of the four FZL-AVF elements is given as $\Phi_{PM} = \sum_{k=1}^4 \Phi_{FZL-AVF}(k) \times M(k)$, where M is a binary random matrix with one-fourth of the pixels carrying a value of 1 and the rest carrying a value of 0 and ' \times ' indicates element-wise multiplication. Then, $\sum_{k=1}^4 M(k) = J$, where J is an all-ones matrix.

A point object located at a distance of z_s with an amplitude $\sqrt{I_s}$ generates a spherical wavefront that is approximated as a parabolic wavefront as the distances are considered large. The complex amplitude at the plane of the phase mask is given as $\sqrt{I_s} C_1 Q\left(\frac{1}{z_s}\right) L\left(\frac{\tilde{r}_s}{z_s}\right)$, and the complex amplitude after the phase mask is given as $\sqrt{I_s} C_1 Q\left(\frac{1}{z_s}\right) L\left(\frac{\tilde{r}_s}{z_s}\right) \exp(i\Phi_{PM})$, where

$L\left(\frac{\bar{s}}{z}\right) = \exp[i2\pi(\lambda z)^{-1}(s_x x + s_y y)]$, $Q(a) = \exp[i\pi a \lambda^{-1}(x^2 + y^2)]$ and C_1 is a complex constant. The intensity distribution obtained at the sensor plane located at a distance of z_h from the phase mask is given as

$$I_{PSF}(\bar{r}_0; \bar{r}_s, z_s) = \left| \sqrt{I_s} C_1 L\left(\frac{\bar{r}_s}{z_s}\right) Q\left(\frac{1}{z_s}\right) \exp(i\Phi_{PM}) \otimes Q\left(\frac{1}{z_h}\right) \right|^2, \quad (3)$$

where $\bar{r}_0 = (u, v)$ is the location vector of the sensor plane and ‘ \otimes ’ represents a 2D convolutional operator. The procedure for combining the four FZL-AVF elements is shown in Fig. 2. The optical configuration of the imaging concept and the 3D intensity distribution for a single object point are shown in Fig. 3. The video of a closer view of the 3D intensity distribution and the rotation of the intensity pattern are given in [Visualization 1](#) and [Visualization 2](#), respectively.

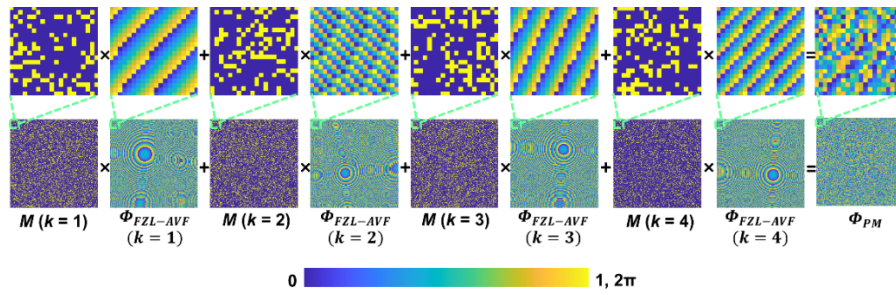


Fig. 2. Procedure for combining four FZL-AVF elements using the random multiplexing method.

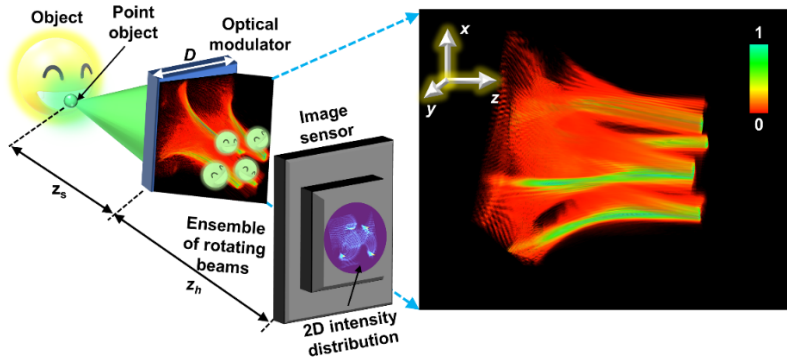


Fig. 3. Optical configuration of the imaging concept and 3D intensity distribution generated by the phase mask for a single point. Supplementary materials on the video of the rotation of the intensity distribution and a closer view of the 3D intensity distributions are given in supplementary materials 1 and 2, respectively. [Visualization 1](#) and [Visualization 2](#).

Since this is a shift-invariant system in the paraxial region, any shift in the location of the point only changes the location of the intensity distribution and not the intensity distribution. This equality is expressed as

$$I_{PSF}(\bar{r}_0; \bar{r}_s, z_s) = I_{PSF}\left(\bar{r}_0 - \frac{z_h}{z_s}\bar{r}_s; 0, z_s\right), \quad (4)$$

where $M_T = \frac{z_h}{z_s}$ is the transverse magnification of the system. A 2D object can be considered a collection of points due to the lack of spatial coherence and can be expressed as

$$o(\bar{r}_s) = \sum_i g_i \delta(\bar{r} - \bar{r}_{s,i}), \quad (5)$$

where g_i 's are real positive constants. The sensor intensity distribution can be given as

$$I_O(\bar{r}_0; z_s) = \sum_i g_i I_{PSF}\left(\bar{r}_0 - \frac{z_h}{z_s} \bar{r}_{s,i}; 0, z_s\right). \quad (6)$$

The image of the object can be reconstructed by correlating $I_O(\bar{r}_0; z_s)$ with $I_{PSF}(\bar{r}_0; z_s)$ as

$$\begin{aligned} P(\bar{r}_R) &= \iint I_O(\bar{r}_0; z_s) I_{PSF}^*(\bar{r}_0 - \bar{r}_R; z_s) d\bar{r}_0 \\ &= \iint \sum_i g_i I_{PSF}\left(\bar{r}_0 - \frac{z_h}{z_s} \bar{r}_{s,i}; z_s\right) I_{PSF}^*(\bar{r}_0 - \bar{r}_R; z_s) d\bar{r}_0 \\ &= \sum_i g_i \Lambda\left(\bar{r}_R - \frac{z_h}{z_s} \bar{r}_{s,i}\right) \approx o\left(\frac{\bar{r}_s}{M_T}\right), \end{aligned} \quad (7)$$

where Λ is a delta-like function.

There are different methods to perform the above correlation using different spatial filters, such as matched filters, phase-only filters, and Weiner filters [37]. Sometimes the image reconstruction can also be estimated by iterative maximum likelihood estimation approaches such as the Lucy-Richardson-Rosen algorithm [28]. However, nonlinear reconstruction (NLR) published in 2018 has a significantly better SNR in comparison to the above methods [18]. With NLR, it is possible to obtain a sharp Λ function with a maximum at (0,0) and approximately 0 elsewhere. The NLR is given as $I_R = \left| \mathcal{F}^{-1} \left\{ |\tilde{I}_{PSF}|^\alpha \exp[i \cdot \arg(\tilde{I}_{PSF})] |\tilde{I}_O|^\beta \exp[-i \cdot \arg(\tilde{I}_O)] \right\} \right|$, where α and β are varied until the lowest reconstruction noise is obtained, \mathcal{F}^{-1} indicates the inverse Fourier transform, \tilde{B} is the Fourier transform of B and $\arg(\cdot)$ is the phase. The lateral and axial resolutions of the system in this case cannot exceed the conventional limits of $\sim 1.22\lambda z_s/D$ and $\sim 8\lambda(z_s/D)^2$, where D is the diameter of the system's aperture.

3. Simulation studies

To understand the performance of the proposed imaging system, we compare four different I-COACH methods: regular I-COACH [17], I-COACH with dot patterns [19], I-COACH with Airy beams [31] and the proposed system I-COACH with self-rotating beams. Two test objects consisting of the words 'CIPHR', 'BGU', and 'PRL' and 'SRM' were used for the simulation studies. A matrix size of 500×500 pixels, pixel size $\Delta = 10 \mu\text{m}$ and $\lambda = 650 \text{ nm}$ was used. It is well established from previous studies [22,27] that the lateral and axial resolutions are independent of the type of deterministic field when the NLR is used for reconstruction. Another recently established finding was that with an increase in the number of beams, there is an improvement in the axial resolution [23,31].

In this study, the SNRs are compared for the above four cases using the test object. In the cases of dot patterns, Airy beams and self-rotating beams, four beams are used, while regular I-COACH was implemented with a random phase mask. The images of the mask patterns, PSFs at two planes, sensor intensity distributions and reconstruction results at the two planes using NLR with $\alpha = 0$ and $\beta = 0.6$ are shown in Fig. 4. The signal is more concentrated for I-COACH with dot patterns and self-rotating patterns than for regular I-COACH and I-COACH with Airy patterns. The average background noise $ABN = \left\{ \sum_{i=1,j=1}^{N,M} I_R(x_i, y_j) \right\} / (N \times M)$, where $I_R(x_i, y_j)$ is the value of pixel (i,j) if and only if pixel (i,j) is in the background of the image. The ABN percentage was estimated for all the above cases as 10.09%, 2.35%, 6.25% and 5.08% for regular I-COACH, I-COACH with dot patterns, I-COACH with Airy patterns and I-COACH with self-rotating

beams, respectively. The case with dot patterns yielded the maximum SNR for one plane, but the reconstruction result was poor for the other plane. Therefore, among the other three methods, the case with self-rotating beams produced the highest SNR. In addition, the energy concentration to small areas in the detector makes it suitable for imaging applications with low-light conditions. The structural similarity index (SSIM) values for regular I-COACH, I-COACH with dot patterns, Airy patterns and self-rotating beams are 0.65, 0.53, 0.32 and 0.47, respectively. Once again, as seen from the SSIM values, I-COACH with self-rotating beams has a higher performance than Airy beams.

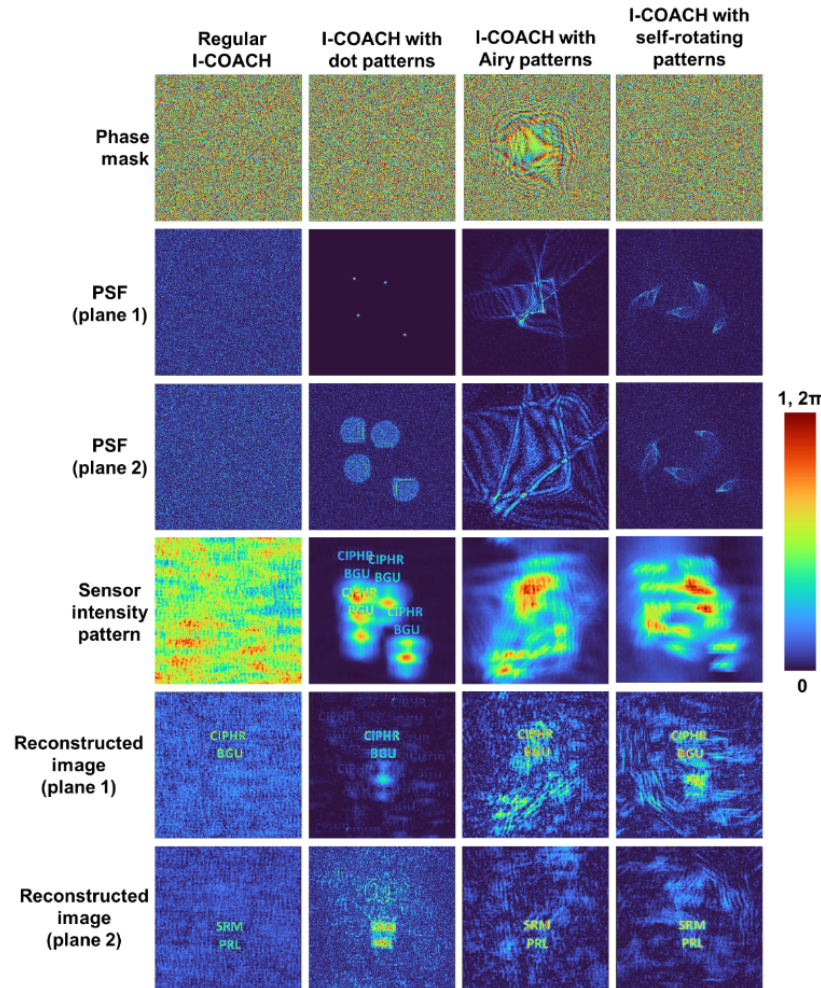


Fig. 4. Simulation results of PSF at two planes, sensor intensity pattern for the test object and reconstruction results for two planes using NLR for $\alpha = 0$ and $\beta = 0.6$ for regular I-COACH, I-COACH with dot patterns, Airy patterns and self-rotating patterns. The color bar indicates the normalized intensity and phase from 0 to 1 and 2π , respectively.

4. Experiments

4.1. Experiments with spatial light modulator

An optical setup was built on an optical table with a high-power LED (Thorlabs, 170 mW, $\lambda = 650$ nm and $\Delta\lambda = 20$ nm), spatial light modulator (SLM) (Thorlabs Exulus HD2, 1920 \times 1200 pixels, pixel size = 8 μm) and an image sensor (Zelux CS165MU/M 1.6 MP monochrome CMOS camera, 1440 \times 1080 pixels with pixel size ~ 3.5 μm). A photograph of the experimental setup is shown in Fig. 5. Light from the high-power LED was polarized along the active axis of the SLM and critically illuminated an object/pinhole using a refractive lens. The PSF was recorded using a pinhole with a diameter of 10 μm . A standard test object (Group 4, Element 4) of the United States Air Force (USAF) resolution target was used as the test object. The light from the object/pinhole was collimated using a refractive lens, reached the beam splitter and was incident on the SLM. On the SLM, phase masks were displayed that modulated light, and the modulated light reached the image sensor. The distance between the SLM and image sensor was ~ 18 cm. A second polarizer oriented along the active axis of the SLM was used to avoid noise entering the image sensor. A bandpass filter was used optionally to reduce the line width to 10 nm.

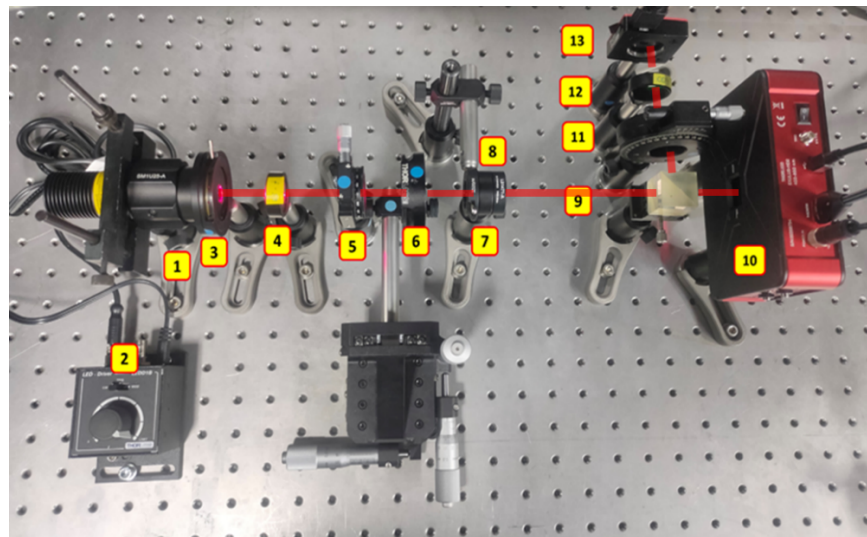


Fig. 5. Photograph of the experimental setup: (1) LED, (2) LED power controller, (3) iris, (4) refractive lens ($f = 50$ mm), (5) polarizer P1, (6) object/pinhole, (7) iris, (8) refractive lens ($f = 50$ mm), (9) beam splitter, (10) SLM, (11) polarizer P2, (12) bandpass filter, and (13) image sensor. Beam path indicated by red semi-transparent line.

In the first step, a direct image was recorded using a phase mask of a diffractive lens with a focal length of 17.8 cm. The images of the phase mask, PSF and sensor intensity distribution are shown in Fig. 6(a)-6(c), respectively. The phase mask for the generation of the Airy pattern, the PSF, the sensor intensity distribution and the reconstruction by NLR are shown in Figs. 7(a)-7(d), respectively. The same set of figures for the case of self-rotating patterns are shown in Figs. 7(e)-7(h). In both cases, the optimal reconstruction was obtained for $\alpha = 0$ and $\beta = 0.6$. The ABN was estimated for both cases, and the ratio between the results of the Airy pattern and self-rotating pattern was approximately two. The SSIM values calculated for the experimental Airy beams and self-rotating beams are 0.6391 and 0.8936, respectively.

The experiment was repeated for a thick object consisting of the USAF object and a pinhole with a diameter of 200 μm separated by a distance of 4 mm. The image of the PSFs recorded at

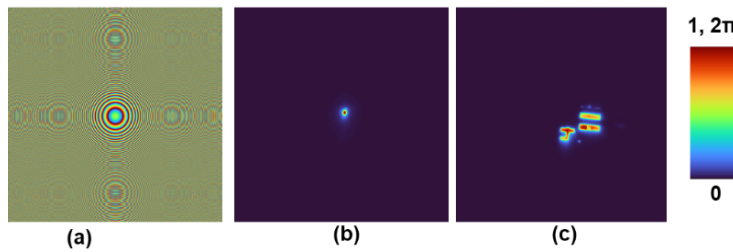


Fig. 6. (a) Phase image of the diffractive lens mask. (b) PSF recorded using a pinhole with a size of $10\text{ }\mu\text{m}$ and (c) direct image of the object. The color bar indicates the normalized intensity and phase from 0 to 1 and 2π , respectively.

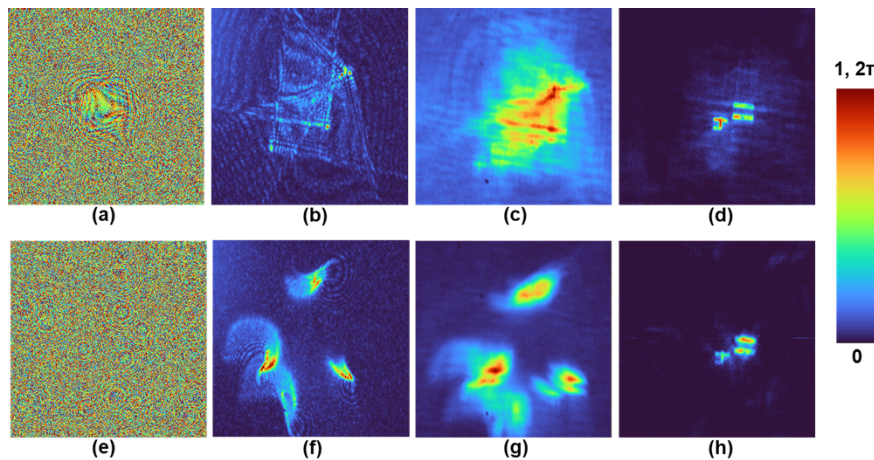


Fig. 7. (a) Phase mask for the generation of the Airy pattern. (b) PSF, (c) sensor intensity distribution and (d) reconstruction by NLR. (e)-(h) Same as (a)-(d) for the generation of the self-rotating pattern. The color bar indicates the normalized intensity and phase from 0 to 1 and 2π , respectively.

the two planes, the hologram of the object and the reconstruction results at the two planes for Airy patterns and self-rotating patterns are shown in Fig. 8. For simplicity, the experiment was carried out in two steps, one for each plane, and the resulting intensity pattern was summed in the computer. Since this is an incoherent imaging system, there is only an addition of intensities and not a complex amplitude, so the above simplified experiment is possible. Once again, it can be seen that the performance of the self-rotating pattern is better than that of the Airy pattern seen from the higher area of dark regions in the background. The experiment was repeated with a thick object formed by two USAF objects (Group 4, Element 4) and (Group – 5, Element 1) separated by a distance of 3 mm. The images of the PSFs of the Airy pattern, self-rotating beams, object hologram of the thick object and reconstruction results for the two planes are shown in Fig. 9.

4.2. Preliminary experiments with diffractive optical elements fabricated using photolithography

To implement I-COACH in a compact system with an ensemble of self-rotating patterns and Airy patterns, diffractive optical elements were fabricated using a rapid photolithography method. The designs were created in MATLAB software and converted into GDSII using LinkCAD software and recalibrated in KLayout Editor with the final version in CIF format. The diffractive optical elements were designed with a pixel size of $8\text{ }\mu\text{m}$, a total of 1200 pixels along the x and y

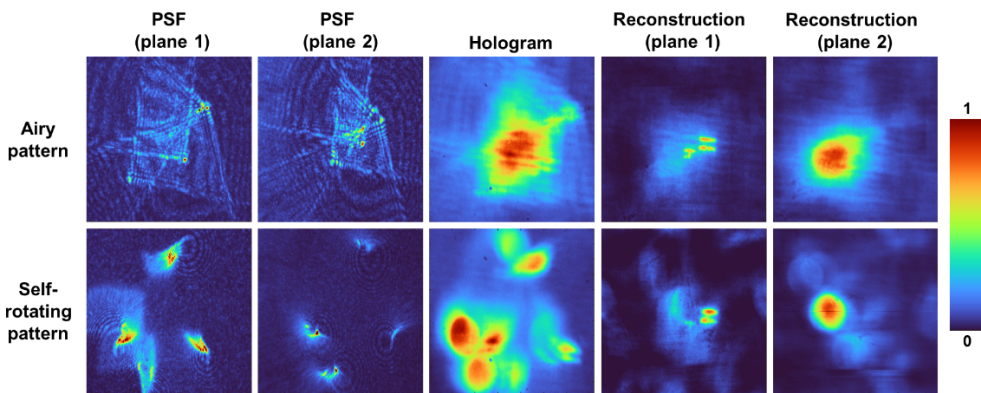


Fig. 8. Images of the recorded PSFs for the Airy pattern and self-rotating patterns for two planes, hologram of the two objects – USAF and pinhole – and reconstruction of the two objects at the two planes. The color bar indicates the normalized intensity from 0 to 1.

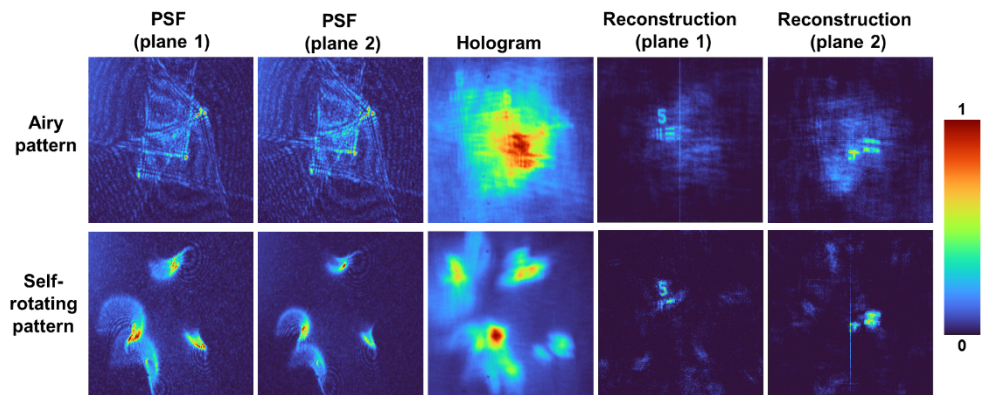


Fig. 9. Images of the recorded PSFs for the Airy pattern and self-rotating patterns for two planes, hologram of the two USAF objects – (Group 4, Element 4) and (Group – 5, Element 1) and reconstruction of the two objects at the two planes. The color bar indicates the normalized intensity from 0 to 1.

directions and a size of $9.6 \text{ mm} \times 9.6 \text{ mm}$. The designs were binarized for easy fabrication, and the resist thickness was set at $t = \lambda/2(n_r - 1)$ to obtain a diffraction efficiency of $\sim 40\%$ [32]. The diffractive elements were fabricated for operation in both reflection and transmission modes on a silica substrate and glass substrate ($T = 180 \mu\text{m}$), respectively, in the ISO5 cleanroom at the Institute of Physics, University of Tartu. A positive photoresist (AR-P 3510 T, Allresist) was spin coated on the substrate at 4000 rpm for 60 s, followed by a soft bake on a hot plate at 100°C for 60 s. A Maskless Aligner (Heidelberg Instruments μMLA) with precise dose control of the light source $\lambda = 390 \text{ nm}$ was used for photoresist exposure. After exposure to UV light, the mask was developed in AR 300-44 (Allresist) and rinsed in ultrapure water [38]. The duration of exposure for a single mask is $\sim 1 \text{ hr}$. The binarized mask patterns for Airy patterns and self-rotating patterns are shown in Figs. 10(a) and 10(b), respectively. The optical microscope images of the central part of the fabricated masks for generating Airy patterns and self-rotating patterns are shown in Figs. 10(c) and 10(d), respectively. The magnified areas indicate a high precision in manufacturing. The fabricated elements were mounted in a modified experimental setup, as

shown in Fig. 11, which is simpler than the one shown in Fig. 5. This setup without an SLM is not polarization dependent, has fewer optical components and is therefore easy to implement.

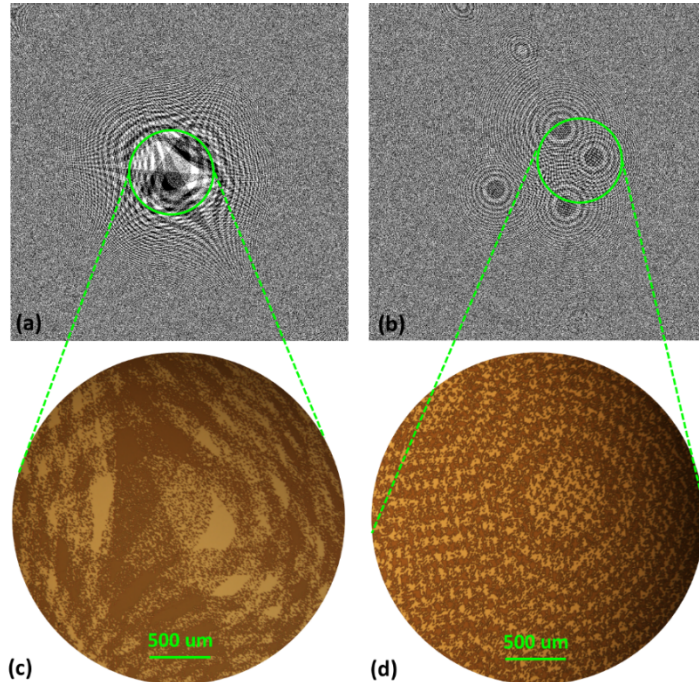


Fig. 10. Images of binarized mask patterns for the generation of (a) Airy beam patterns and (b) self-rotating beam patterns. Optical microscope images of the central parts of masks for generation of (c) Airy beam patterns and (d) self-rotating beam patterns. The darker regions of (c) and (d) indicate resist removal, and the brighter regions indicate remaining resist.

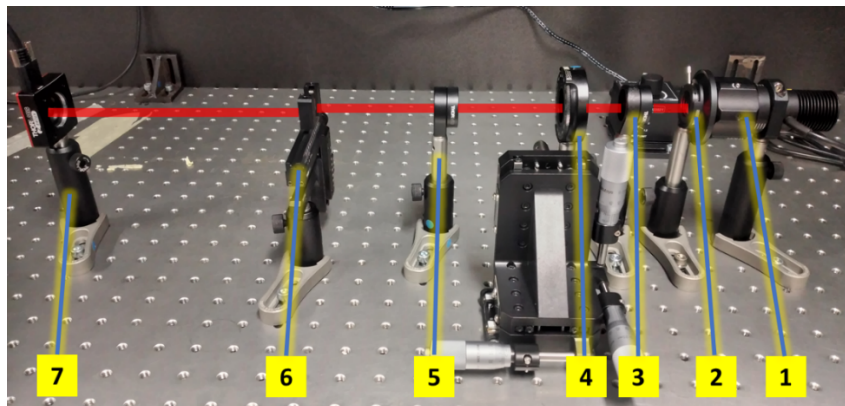


Fig. 11. Photograph of the optical setup for testing the fabricated diffractive element: (1) LED, (2) iris, (3) refractive lens for illumination, (4) object, (5) refractive lens for collimation, (6) fabricated diffractive element and (7) image sensor.

Light from a high-power LED (Thorlabs, 170 mW, $\lambda = 650 \text{ nm}$ and $\Delta\lambda = 20 \text{ nm}$) critically illuminates an object with a refractive lens of focal length 5 cm. The light from the object was

collimated by a refractive lens, incident on the fabricated diffractive optical element and recorded by an image sensor (Zelux CS165MU/M 1.6 MP monochrome CMOS camera, 1440×1080 pixels with pixel size $\sim 3.5 \mu\text{m}$). In the first step, the PSF was recorded using a pinhole with a diameter of $25 \mu\text{m}$. In the next step, a circular object with a diameter of $200 \mu\text{m}$ was recorded. The images of the PSF, object intensity pattern and reconstruction for Airy patterns are shown in the upper line of Fig. 12. The images of the PSF, object intensity pattern and reconstruction for self-rotating patterns are shown in the lower line of Fig. 12. Since the manufactured diffractive element is a binary element $[0, \pi]$, higher diffraction orders are generated, which leads to a higher noise level compared to the case with SLM. In addition to NLR, a median filter and raising images to power p ($p = 2$) were used to improve the reconstruction results [22]. Once again, the background noise for self-rotating beams is lower than that for Airy patterns.

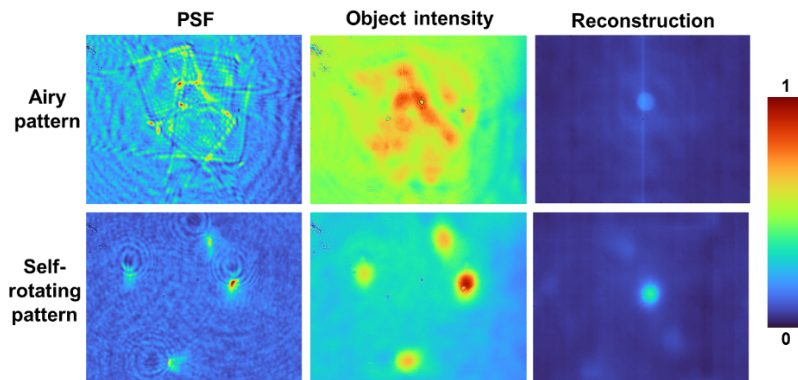


Fig. 12. Images of the recorded PSF, object intensity for the Airy pattern and self-rotating patterns for a circular object with a diameter of $200 \mu\text{m}$. The color bar indicates the normalized intensity from 0 to 1.

5. Summary and conclusions

The I-COACH technique revolutionized the field of incoherent holography. In the first version of I-COACH, the light from an object was modulated by a quasi-random phase mask, and the intensity distribution was recorded. From this intensity recording and the PSFs recorded at multiple planes, a 3D image of the object can be reconstructed. I-COACH evolved with a better SNR using advanced computational reconstruction methods such as NLR and by replacing the quasi-random phase mask with masks that generate sparse random arrays of dot patterns. However, in the case with dot patterns, it is necessary to multiplex several mask patterns to image at different depths. Recently, a sparse random array of Airy patterns was implemented in I-COACH with an improved SNR.

In this study, a sparse random array of self-rotating beams was used for implementing I-COACH. Unlike Airy patterns, self-rotating patterns are concentrated in smaller areas in the image sensor and are not shifted but rotated with depth, resulting in an improved SNR. Both 2D and 3D experiments were carried out, which demonstrated the better performance of self-rotating patterns in comparison to Airy patterns in SNR. Large-area ($\sim 10 \text{ mm}$) diffractive elements for the generation of sparse Airy patterns and self-rotating patterns were fabricated using photolithography. Preliminary optical experiments were carried out in a simple experimental setup using the fabricated diffractive elements, and the results once again confirmed the better performance of self-rotating beams in comparison to Airy beams. However, improved design and manufacturing of greyscale diffractive elements are needed to improve the SNR to the level of SLM and improve the diffraction efficiency. This new advancement may enable the

implementation of I-COACH in light-sensitive application areas. It is common in indirect imaging methods such as computational imaging and digital holography to generate images that are slightly noisier than the direct imaging counterparts, which can be suppressed using numerous noise reduction methods [39,40].

In Figs. 7 and 9, it appears that the resolution of Airy and self-rotating beams is different. That is due to the presence of localized reconstruction noises that can be shifted to a different location by a suitable choice of beam locations. The holographic blurring occurring due to the reconstruction of an object plane by a PSF corresponding to another plane is not uniform in the case of self-rotating patterns, unlike the Airy pattern and direct imaging. The reconstructions in both cases are still not as good as direct imaging, so it is necessary to look for better ingredients for ensemble and improved computational reconstruction methods. Further studies on I-COACH are needed with different characteristics of Airy beams and self-rotating beams, different object sizes, computational algorithms and their relation to resolution and SNR for improved implementation of I-COACH. With recent developments in the generation of exotic beams, we believe that it is possible to create advanced incoherent imaging technologies [41,42].

Funding. Estonian Research Competency Council (PRG753); European Regional Development Fund (TK134); HORIZON EUROPE Widening Participation and Strengthening the European Research Area (857627 (CIPHR)).

Acknowledgments. This work was also supported by the ERDF project's Center of Technologies and Investigations of Nanomaterials (NAMUR+, project number 2014-2020.4.01.16-0123). The research was conducted using the NAMUR+ core facility funded by the Estonian Research Council (TT 13).

Disclosures. The authors declare no conflicts of interest.

Data availability. Data underlying the results presented in this paper are not publicly available at this time but may be obtained from the authors upon reasonable request.

References

1. H. H. Barrett and K. J. Myers, *Foundations of Image Science*, Wiley Series in Pure and Applied Optics (Wiley, 2004).
2. J. W. Goodman and R. W. Lawrence, "Digital image formation from electronically detected holograms," *Appl. Phys. Lett.* **11**(3), 77–79 (1967).
3. M. K. Kim, *Digital Holography and Microscopy: Principles, Techniques and Applications*, (Springer Verlag, 2011).
4. W. Osten, A. Faridian, P. Gao, K. Körner, D. Naik, G. Pedrini, A. K. Singh, M. Takeda, and M. Wilke, "Recent advances in digital holography [Invited]," *Appl. Opt.* **53**(27), G44–G63 (2014).
5. J. Rosen, A. Vijayakumar, M. Kumar, M. R. Rai, R. Kelner, Y. Kashter, A. Bulbul, and S. Mukherjee, "Recent advances in self-interference incoherent digital holography," *Adv. Opt. Photonics* **11**(1), 1–66 (2019).
6. N. T. Shaked, B. Katz, and J. Rosen, "Review of three-dimensional holographic imaging by multiple-viewpoint-projection based methods," *Appl. Opt.* **48**(34), H120–H136 (2009).
7. J. P. Liu, T. Tahara, Y. Hayasaki, and T. C. Poon, "Incoherent digital holography: a review," *Appl. Sci.* **8**(1), 143 (2018).
8. J. Rosen and G. Brooker, "Digital spatially incoherent Fresnel holography," *Opt. Lett.* **32**(8), 912–914 (2007).
9. G. Brooker, N. Siegel, V. Wang, and J. Rosen, "Optimal resolution in Fresnel incoherent correlation holographic fluorescence microscopy," *Opt. Express* **19**(6), 5047–5062 (2011).
10. J. Rosen, N. Siegel, and G. Brooker, "Theoretical and experimental demonstration of resolution beyond the Rayleigh limit by FINCH fluorescence microscopic imaging," *Opt. Express* **19**(27), 26249–26268 (2011).
11. N. Siegel and G. Brooker, "Improved axial resolution of FINCH fluorescence microscopy when combined with spinning disk confocal microscopy," *Opt. Express* **22**(19), 22298–22307 (2014).
12. A. Bulbul, N. Hai, and J. Rosen, "Coded aperture correlation holography (COACH) with a superior lateral resolution of FINCH and axial resolution of conventional direct imaging systems," *Opt. Express* **29**(25), 42106–42118 (2021).
13. V. Anand, T. Katkus, S. H. Ng, and S. Juodkazis, "Review of Fresnel incoherent correlation holography with linear and non-linear correlations [Invited]," *Chin. Opt. Lett.* **19**(2), 020501 (2021).
14. T. Tahara, Y. Kozawa, A. Ishii, K. Wakunami, Y. Ichihashi, and R. Oi, "Two-step phase-shifting interferometry for self-interference digital holography," *Opt. Lett.* **46**(3), 669–672 (2021).
15. A. Vijayakumar, Y. Kashter, R. Kelner, and J. Rosen, "Coded aperture correlation holography—a new type of incoherent digital holograms," *Opt. Express* **24**(11), 12430–12441 (2016).
16. A. Vijayakumar, Y. Kashter, R. Kelner, and J. Rosen, "Coded aperture correlation holography (COACH) system with improved performance [Invited]," *Appl. Opt.* **56**(13), F67–F77 (2017).
17. A. Vijayakumar and J. Rosen, "Interferenceless coded aperture correlation holography—a new technique for recording incoherent digital holograms without two-wave interference," *Opt. Express* **25**(12), 13883–13896 (2017).

18. M. R. Rai, A. Vijayakumar, and J. Rosen, "Non-linear adaptive three-dimensional imaging with interferenceless coded aperture correlation holography (I-COACH)," *Opt. Express* **26**(14), 18143–18154 (2018).
19. M. R. Rai and J. Rosen, "Noise suppression by controlling the sparsity of the point spread function in interferenceless coded aperture correlation holography (I-COACH)," *Opt. Express* **27**(17), 24311–24323 (2019).
20. Y. Wan, C. Liu, T. Ma, Y. Qin, and S. Lv, "Incoherent coded aperture correlation holographic imaging with fast adaptive and noise-suppressed reconstruction," *Opt. Express* **29**(6), 8064–8075 (2021).
21. V. Anand, J. Rosen, and S. Juodkazis, "Review of engineering techniques in chaotic coded aperture imagers," *Light: Adv. Manuf.* **3**, 1–13 (2022).
22. D. Smith, S. Gopinath, and F. G. Arockiaraj, *et al.*, "Nonlinear reconstruction of images from patterns generated by deterministic or random optical masks—concepts and review of research," *J. Imaging* **8**(6), 174 (2022).
23. V. Anand, "Tuning axial resolution independent of lateral resolution in a computational imaging system using Bessel speckles," *Micromachines* **13**(8), 1347 (2022).
24. G. A. Siviloglou, J. Broky, A. Dogariu, and D. N. Christodoulides, "Observation of accelerating Airy beams," *Phys. Rev. Lett.* **99**(21), 213901 (2007).
25. J. Broky, G. A. Siviloglou, A. Dogariu, and D. N. Christodoulides, "Self-healing properties of optical Airy beams," *Opt. Express* **16**(17), 12880–12891 (2008).
26. N. K. Efremidis, Z. Chen, M. Segev, and D. N. Christodoulides, "Airy beams and accelerating waves: an overview of recent advances," *Optica* **6**(5), 686–701 (2019).
27. V. Anand, S. Khonina, R. Kumar, N. Dubey, A. Reddy, J. Rosen, and S. Juodkazis, "Three-dimensional incoherent imaging using spiral rotating point spread functions created by double-helix beams," *Nanoscale Res. Lett.* **17**(1), 37 (2022).
28. V. Anand, M. Han, J. Maksimovic, S. H. Ng, T. Katkus, A. Klein, K. Bamberg, M. J. Tobin, J. Vongsivut, and S. Juodkazis, "Single-shot mid-infrared incoherent holography using Lucy-Richardson-Rosen algorithm," *Opto-Electron. Sci.* **1**(3), 210006 (2022).
29. K. Niu, S. Zhao, Y. Liu, S. Tao, and F. Wang, "Self-rotating beam in the free space propagation," *Opt. Express* **30**(4), 5465–5472 (2022).
30. K. Niu, Y. Zhai, and F. Wang, "Self-healing property of the self-rotating beam," *Opt. Express* **30**(17), 30293–30302 (2022).
31. R. Kumar, V. Anand, and J. Rosen, "3D single shot lensless incoherent optical imaging using coded phase aperture system with point response of scattered airy beams," *Sci. Rep.* **13**(1), 2996 (2023).
32. A. Vijayakumar and S. Bhattacharya, *Design and Fabrication of Diffractive Optical Elements with MATLAB* (SPIE, 2017).
33. N. Davidson, A. A. Friesem, and E. Hasman, "Holographic axilens: high resolution and long focal depth," *Opt. Lett.* **16**(7), 523–525 (1991).
34. J. Sochacki, S. Bará, Z. Jaroszewicz, and A. Kołodziejczyk, "Phase retardation of the uniform-intensity axilens," *Opt. Lett.* **17**(1), 7–9 (1992).
35. J. H. McLeod, "The axicon: A new type of optical element," *J. Opt. Soc. Am.* **44**(8), 592–597 (1954).
36. S. Bara, C. Frere, Z. Jaroszewicz, A. Kołodziejczyk, and D. Leseberg, "Modulated on-axis circular zone plates for a generation of three-dimensional focal curves," *J. Mod. Opt.* **37**(8), 1287–1295 (1990).
37. A. Vijayakumar and S. Bhattacharya, "Characterization and correction of spherical aberration due to glass substrate in the design and fabrication of Fresnel zone lenses," *Appl. Opt.* **52**(24), 5932–5940 (2013).
38. S. Gopinath, P. P. Angamuthu, T. Kahro, A. Bleahu, F. G. Arockiaraj, D. Smith, S. H. Ng, S. Juodkazis, K. Kukli, A. Tamm, and V. Anand, "Implementation of a large-area diffractive lens using multiple sub-aperture diffractive lenses and computational reconstruction," *Photonics* **10**(1), 3 (2022).
39. V. Bianco, P. Memmolo, M. Leo, S. Montresor, C. Distante, M. Paturzo, P. Picart, B. Javidi, and P. Ferraro, "Strategies for reducing speckle noise in digital holography," *Light: Sci. Appl.* **7**(1), 48 (2018).
40. G. Situ, "Deep holography," *Light: Adv. Manuf.* **3**(2), 1 (2022).
41. K. Niu, Y. Liu, Z. Chu, Q. Tian, X. He, C. Pan, and F. Wang, "Controllable self-rotating array beam with an arc-shaped accelerating trajectory," *Opt. Express* **31**(8), 12150–12161 (2023).
42. Y. Shen, X. Yang, D. Naidoo, X. Fu, and A. Forbes, "Structured ray-wave vector vortex beams in multiple degrees of freedom from a laser," *Optica* **7**(7), 820–831 (2020).